Available online at www.sciencedirect.com
ScienceDirect
Trans. Nonferrous Met. Soc. China 35(2025) 1772−1786
Transactions of Nonferrous Metals Society of China
www.tnmsc.cn

Synchronous enhancement of corrosion resistance and mechanical properties of Mg−Zn−Ca alloys by grain refinement using equal channel angular pressing

Yi-zhuo WANG[1], Xiao-ping LUO[2], Gang-xiao REN[3], Hong-xia WANG[1], Li-fei WANG[1], Wei-li CHENG[1], Hang LI[1], Xiao-peng LU[4], Kwang-seon SHIN[5]

1. College of Materials Science and Engineering, Shanxi Key Laboratory of Magnesium Matrix Materials, Taiyuan University of Technology, Taiyuan 030024, China;
2. College of Materials Science and Engineering, Taiyuan University of Science and Technology, Taiyuan 030024, China;
3. Shanxi Jianghuai Heavy Industry Co., Ltd., Jincheng 048000, China;
4. School of Materials Science and Engineering, Northeastern University, Shenyang 110819, China;
5. Magnesium Technology Innovation Center, School of Materials Science and Engineering, Seoul National University, Gwanak-ro, Gwanak-gu, Seoul 08826, Korea

Received 7 October 2023; accepted 9 April 2024

Abstract: To investigate the effect of microstructure evolution on corrosion behavior and strengthening mechanism of Mg−1Zn−1Ca (wt.%) alloys, as-cast Mg−1Zn−1Ca alloys were performed by equal channel angular pressing (ECAP) with 1 and 4 passes. The corrosion behavior and mechanical properties of alloys were investigated by optical microscopy (OM), scanning electron microscopy (SEM), electron backscatter diffraction (EBSD), electrochemical tests, immersion tests and tensile tests. The results showed that mechanical properties improved after ECAP 1 pass; however, the corrosion resistance deteriorated due to high-density dislocations and fragmented secondary phases by ECAP. In contrast, synchronous improvement in the mechanical properties and corrosion resistance was achieved though grain refinement after ECAP 4 passes; fine grains led to a significant improvement in the yield strength, ultimate tensile strength, elongation, and corrosion rate of 103 MPa, 223 MPa, 30.5%, and 1.5843 mm/a, respectively. The enhanced corrosion resistance was attributed to the formation of dense corrosion product films by finer grains and the barrier effect by high-density grain boundaries. These results indicated that Mg−1Zn−1Ca alloy has a promising potential for application in biomedical materials.

Key words: Mg−1Zn−1Ca alloy; equal channel angular pressing; grain refinement; corrosion behavior; mechanical properties

1 Introduction

Since the implementation of a stringent national family planning policy, individuals requiring contraception have successfully been able to use intrauterine devices (IUDs) in a consistent manner. Conventional IUDs are typically inert and non-degradable, and made of materials such as stainless steel, plastic, copper-bearing materials, and cobalt-based alloys [1]. These IUDs require subsequent removal surgeries when they are no longer suitable for the human body or when the users want to conceive. Consequently, frequent IUD

Corresponding author: Hong-xia WANG, Tel: +86-13233686858, E-mail: wanghxia1217@163.com
https://doi.org/10.1016/S1003-6326(25)66782-3
1003-6326/© 2025 The Nonferrous Metals Society of China. Published by Elsevier Ltd & Science Press
This is an open access article under the CC BY-NC-ND license (http://creativecommons.org/licenses/by-nc-nd/4.0/)

removal not only inflicts discomfort on patients but also increases healthcare costs. Moreover, the degradation or wear of these conventional materials may lead to the release of toxic ions, which can trigger inflammation and disease in the human body, such as the burst release of cupric ions [2]. As the Chinese government recently introduced a three-child policy that allows couples to have up to three children, various supportive measures have been taken to incentivize childbirth. Therefore, there is a high demand for short-term degradable IUDs that have a lifespan of one or two years. Mg alloys are favored by their biocompatibility and degradability [3−6]. Due to the current shortage of short-term IUDs on the market, their performance standards are not yet clear. The study focused on improving the corrosion resistance and mechanical properties of Mg alloys remains an emphasis of this research.

Mg is one of the most essential elements required for human metabolism, and Mg alloys are considered potential materials for body implants owing to their biocompatibility and degradability. However, many studies on biomedical Mg alloys have focused on Mg−rare earth (Mg−RE) alloys. RE elements improve the microstructure and overall properties of Mg alloys [7,8]. Nevertheless, the safety of using RE elements in body implants has not yet been fully evaluated. Particularly, the addition of Zn to Mg alloys has been shown to impart antibacterial properties, whereas Ca is a crucial component of the human bone and plays a vital role in chemical signaling within cells [9,10]. However, their poor mechanical properties and high degradation rates are two major problems that limit their applications. One of the most employed strategies to enhance the strength of Mg alloys is grain refinement. Mechanical properties are significantly improved by grain refinement strengthening. Furthermore, the grain size can also influence the alloy's corrosion resistance.

RALSTON et al [11] developed an equation, which follows a Hall−Petch type relationship, to explain the impact of grain size on corrosion resistance. Among the various methods of severe plastic deformation (SPD), equal channel angular pressing (ECAP) is particularly effective in achieving high accumulative strain and grain refinement. TORKIAN et al [12] demonstrated that ECAP significantly enhanced the corrosion resistance of the WE43 Mg alloy in vivo degradation test. GUI et al [13] observed that the corrosion rate of a Mg−Gd−Zn−Zr−Mn alloy decreased after ECAP treatment, and the alloy had good corrosion resistance. As a result of these findings, numerous researchers have recognized the benefits of grain size reduction through SPD for enhancing the corrosion resistance of Mg alloys. However, a definitive understanding of the corrosion behavior and degradation mechanism of Mg alloys with fine-grained structures produced via SPD remains elusive.

Hence, in this study, ECAP as the SPD method for manufacturing Mg−1Zn−1Ca (ZX11, wt.%) alloy was employed with different passes. By refining grains, this method not only improves the mechanical properties but also enhances the corrosion resistance of the alloy. Moreover, the microstructure evolution, mechanical properties variation trend, and corrosion behavior of the alloy were investigated.

2 Experimental

2.1 Material preparation

The cast ZX11 alloy was fabricated using pure Mg (99.99%), pure Zn (99.99%), and Mg−30Ca (wt.%). First, the raw materials were melted in an electric resistance furnace and then held at 720 °C for 30 min. Subsequently, a gas mixture of CO_2 and SF_6 was injected into the furnace during melting to prevent the alloy from being overburned. Finally, after preheating the mold at 200 °C, the melt was poured into the mold and cooled to room temperature (25 °C).

The alloy was cut into specimens of 10 mm × 10 mm × 64 mm and subjected to ECAP treatment with 1 and 4 passes, respectively, using the B_c route (a method of applying SPD to metal alloys by passing them through a die with a sharp angle and rotating them 90° clockwise after each pass) at 350 °C, as shown in Fig. 1. Graphite was used for lubrication to reduce the friction between the specimen and the inner wall of the mold.

2.2 Electrochemical test

The electrochemical behavior of the ZX11 alloys was investigated using potentiodynamic polarization (PDP) and electrochemical impedance spectroscopy (EIS) with a three-electrode CH350H

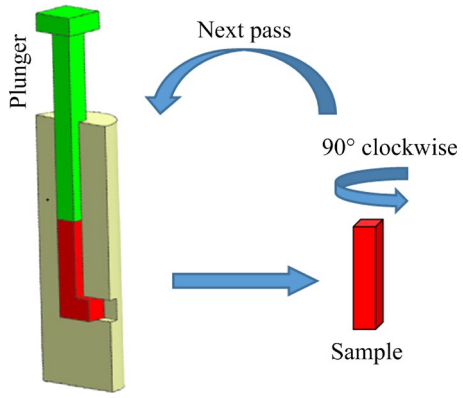

Fig. 1 Schematic diagram of ECAP process

electrochemical workstation. The three-electrode system consisted of a saturated calomel electrode (SCE) as the reference electrode (RE), a Pt sheet as the auxiliary electrode (AE), and the alloy as the working electrode (WE). The exposed area of the WE was 10 mm × 10 mm. All specimens were tested in simulated body fluid (SBF) at room temperature (25 °C). The specimens were immersed in SBF for 1 h to form a stable electrochemical system. EIS measurements were performed at a frequency range of $1\times(10^{6}-10^{-2})$ Hz, using a sinusoidal perturbation amplitude of 10 mV. The polarization tests were conducted at scanning potentials from −2 to −1 V (vs SCE) and a scanning rate of 0.5 mV/s. The electrochemical tests were repeated at least three times. Zsimpwin software was used to analyze experimental data.

2.3 Immersion test

To determine the mass loss, the specimens were immersed in a constant-temperature water bath containing the SBF (pH 7.4) at 37 °C. Its composition is listed in Table 1.

Table 1 Composition of SBF

Composition	Content/(g·L^{-1})
NaCl	8.00
KCl	0.40
$NaHCO_3$	0.35
$CaCl_2$	0.14
$MgCl_2·6H_2O$	0.10
$MgSO_4·7H_2O$	0.06
KH_2PO_4	0.06
$Na_2HPO_4·12H_2O$	0.06

The SBF was replaced every 24 h to maintain its composition and pH. After immersion, the specimens were rinsed with distilled water and immersed in a solution of chromic acid (200 g/L H_2CrO_4) for 10 min to remove the corrosion products. The corrosion morphology of the alloys was observed using a scanning electron microscope. The mass of each specimen was measured before and after immersion and the average corrosion rate was calculated using the mass loss method using Eq. (1) [14]:

$$C_R=\frac{8.64\times10^4\Delta m}{ADT} \quad (1)$$

where C_R is the average corrosion rate (mm/a), Δm is the mass loss (mg), A is the surface area of the specimen (cm^2), D is the density of the Mg alloy (g/cm^3), and T is the immersion time (d).

2.4 Mechanical test

Tensile specimens were cut using a wire-cutting machine (DK7725). The tensile direction was parallel to the extrusion direction (ED) of the ECAP. Universal testing machine (DNS100) was used to test the mechanical properties of the tensile specimens at a speed of 0.2 mm/min. The ultimate tensile strength, yield strength, and elongation were recorded. The exhibited typical tensile curves were repeatedly tested at least three times.

2.5 Microstructural characterization

Optical microscopy (OM, Leica 2700M), scanning electron microscopy (SEM, MIRE3 TESCAN), X-ray diffraction (XRD, TD−3500), and electron back-scattered diffraction (EBSD, c-swift) were used to characterize the microstructures of the as-cast and ECAP-treated alloys. The surface of the specimen observed for microstructural characterization was perpendicular to the ED of ECAP. The specimens for EBSD observations were electron-polished in an AC_2 solution at −20 °C.

3 Results and discussion

3.1 Microstructural evolution

Figure 2 shows the OM and SEM images as well as XRD patterns of the as-cast and ECAP-treated ZX11 alloys. The microstructure of the alloy was significantly refined by ECAP. In particular, the as-cast ZX11 alloy (Fig. 2(a)) had

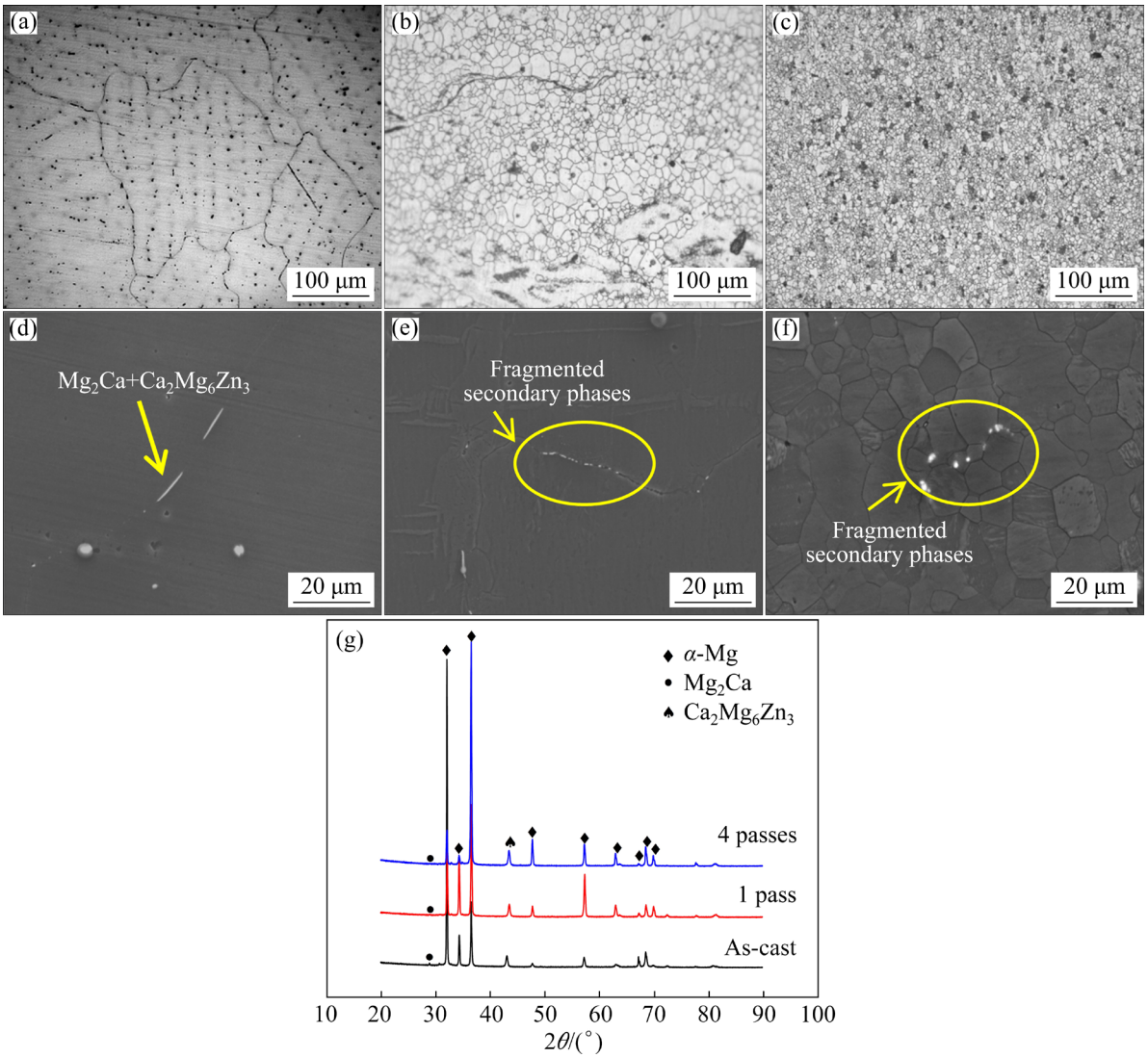

Fig. 2 Microstructures (a−f) and XRD patterns (g) of as-cast and ECAP-treated ZX11 alloys: (a, d) As-cast; (b, e) 1 pass; (c, f) 4 passes

coarse grains with a large grain size and dotted secondary phases that were randomly distributed inside the grains or along grain boundaries. The XRD patterns (Fig. 2(g)) reveals that the secondary phases mainly consist of Mg_2Ca phase and $Ca_2Mg_6Zn_3$ phase, and these phases did not change after ECAP. After ECAP 1 pass (Fig. 2(b)), the microstructure consisted of fine equiaxed grains and coarse grains, forming a mixed microstructure. The semi-continuous secondary phases at grain boundaries were fractured into discrete particles (Fig. 2(e)). After ECAP 4 passes (Fig. 2(c)), the grains became finer and more uniform, and secondary phases became more dispersed. The secondary phases that distributed at the grain boundaries were also more fragmented (Fig. 2(f)).

Figure 3 exhibits the EBSD inverse pole figure (IPF) and grain size distribution of the ECAP-treated alloys. EBSD IPF maps were used to represent different grain orientations. Different colors represent different grain orientations. The angle between the ED and ⟨0001⟩ and the angle between ED and ⟨1010⟩ are denoted by θ and φ, respectively. Grains with $\theta < 60°$ are referred to as (0001) grains. In the range of $60° \leq \theta \leq 90°$, grains with $0 \leq \varphi < 15°$ are referred to as (1010) grains and grains with $15° \leq \varphi \leq 30°$ are referred to as $(11\bar{2}0)$ grains [15]. After ECAP 1 pass, the grain orientation became more random, and there was no clear preferential direction. The microstructure could be characterized by both fine dynamic recrystallization (DRX) grains and coarse deformed

grains, resulting in a mixed microstructure with an average grain size of 18.46 μm. After ECAP 4 passes, the alloy exhibited a homogeneously fine equiaxed grain structure (Fig. 3(b)). The coarse deformed grains were replaced by fine DRX grains, leading to a significant reduction in grain size to 9.24 μm.

Figure 4 shows the pole figures (PFs) of ECAP-treated alloys, which reflect the texture evolution of the material. With each additional pass,

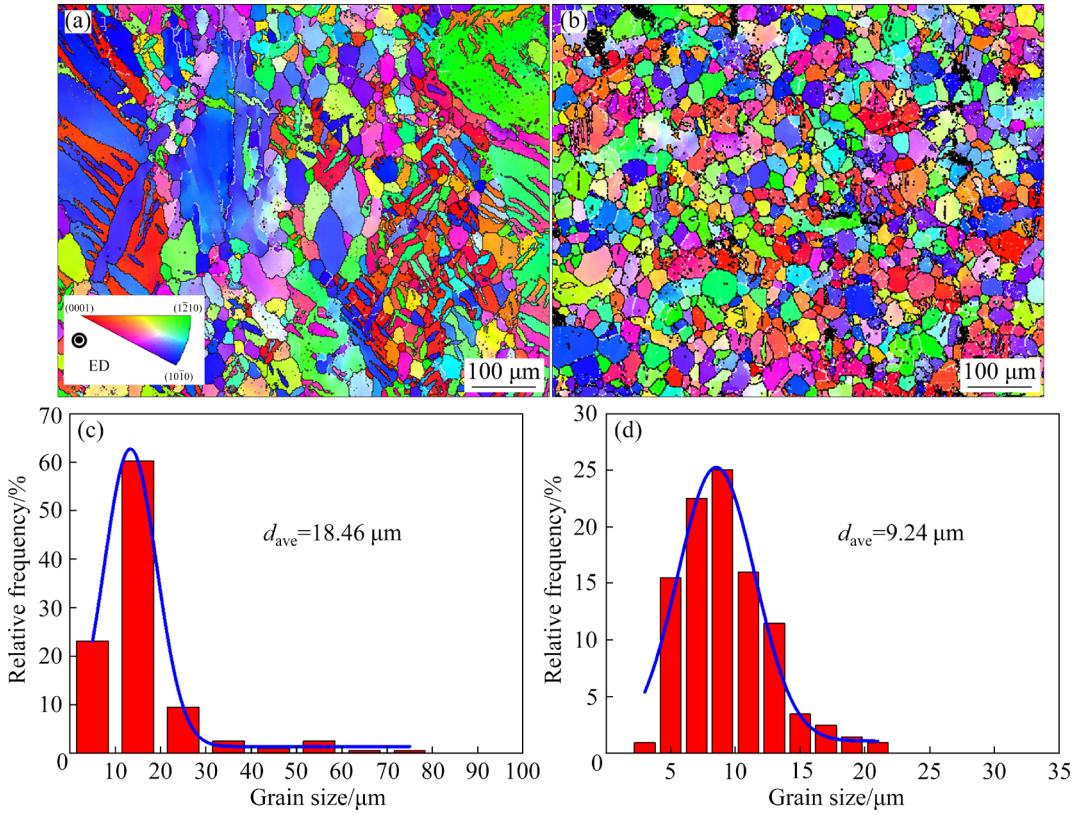

Fig. 3 EBSD IPF maps (a, b) and grain size distributions (c, d) of ECAP-treated ZX11 alloys: (a, c) 1 pass; (b, d) 4 passes

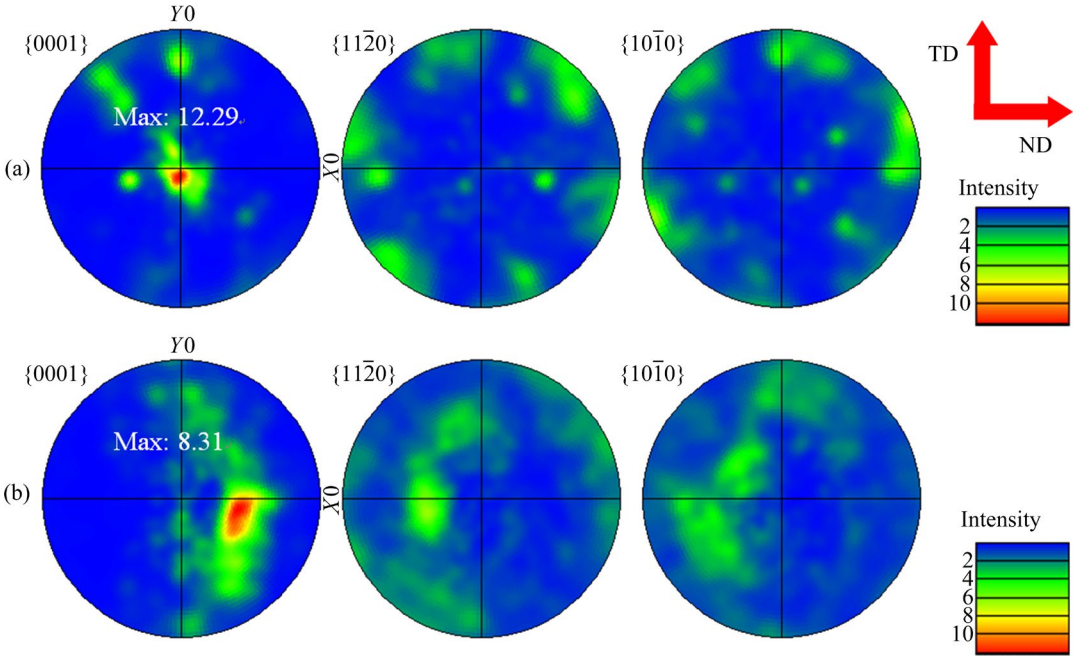

Fig. 4 Pole figures of ECAP-treated ZX11 alloys: (a) 1 pass; (b) 4 passes

the microstructure of the ZX11 alloy becomes increasingly refined. The microstructure of the ZX11 alloy after ECAP 1 pass had a typical basal rolling texture, with most grains having their ⟨0001⟩ direction parallel to ED. The corresponding maximum texture density was 12.29 (Fig. 4(a)). The region with the maximum texture density was centered on the (0001) PF, indicating that the (0001) basal plane was perpendicular to the ED. After ECAP 4 passes, the grains experienced rotation and shear deformation, which changed their microstructure and texture [16]. Most grains had slight deflection angles of their (0001) basal plane towards the transverse direction (TD). Consequently, the texture distribution became more diffuse, and the maximum texture density decreased to 8.31 (Fig. 4(b)). This indicates that the ZX11 alloy underwent texture weakening after ECAP 4 passes compared to ECAP 1 pass. This can be attributed to the replacement of nearly all coarse deformed grains by DRX grains with a relatively random orientation, which weakens the texture and improves the formability [17].

Figure 5 demonstrates the Schmid factor distribution for $(0001)\langle 11\bar{2}0\rangle$ basal slip of the ECAP alloy. The results showed that the average Schmid factor increased after ECAP 4 passes. The dominant deformation mechanism in Mg alloys [18] is basal slip because the critical resolved shear stress (CRSS) of a non-basal slip system is 100 times higher than that of a basal slip system at room temperature, which makes it difficult to activate non-basal slip. A higher Schmid factor indicates that a lower CRSS is required for basal slip, which implies that the alloy enters the yield stage earlier and has a lower yield strength [17]. After ECAP 4 passes, the Schmid factor increases to 0.38 (Fig. 5(b)), the texture displays a tendency towards a softly-orientation, which is advantageous for promoting basal slip.

Figure 6 shows kernel average misorientation (KAM) results of the ECAP-treated ZX11 alloys, which reflect the dislocation density and distribution in the material. The as-cast alloy undergoes work hardening after ECAP 1 pass, leading to the introduction of defects such as dislocations. Hence, the dislocation density rapidly increases, compared with as-cast ZX11 alloy [19]. After ECAP 4 passes, dislocations disappeared while dynamic recrystallization occurred during thermal deformation [20], resulting in a slight decrease in the KAM value to 0.74° (Figs. 6(b, d)). At the early stage of deformation, the dislocations multiply quickly and the accumulated distortion energy provides the driving force for dynamic recrystallization [21]. The undistorted grains assimilated the distorted grains that were formed during the deformation process. This led to a higher rate of dislocation disappearance than that of dislocation generation during the dynamic recrystallization process, resulting in a slight reduction in dislocation density.

3.2 Corrosion behavior of ZX11 alloys

Figure 7 shows the corrosion morphology and EDS results of the as-cast and ECAP-treated ZX11 alloys after immersion in SBF for 3 d. The alloy surfaces exhibited different degrees of corrosion after immersion. The surface of the as-cast alloy was degraded and covered with corrosion products

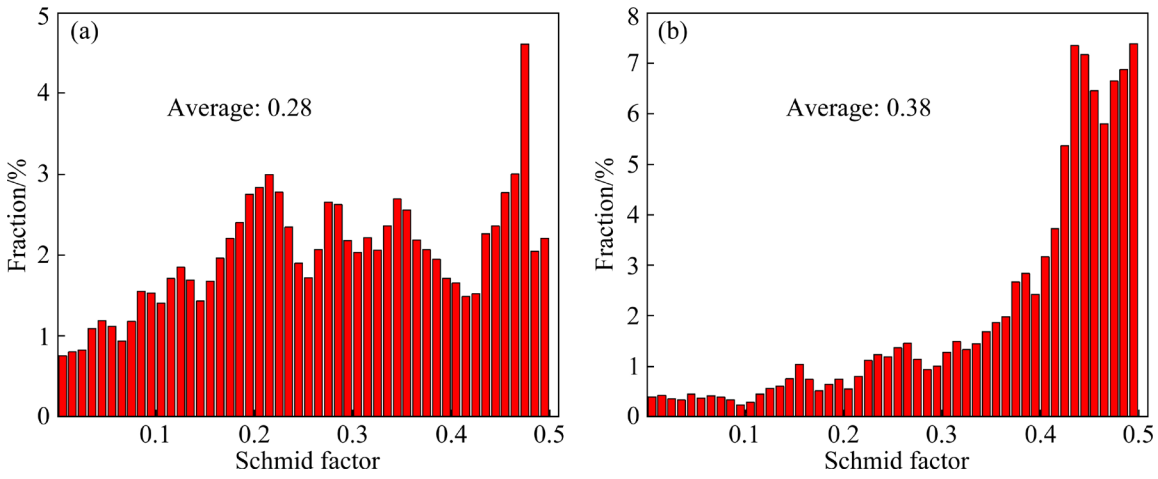

Fig. 5 Distribution of $(0001)\langle 11\bar{2}0\rangle$ Schmid factor of ECAP-treated ZX11 alloys: (a) 1 pass; (b) 4 passes

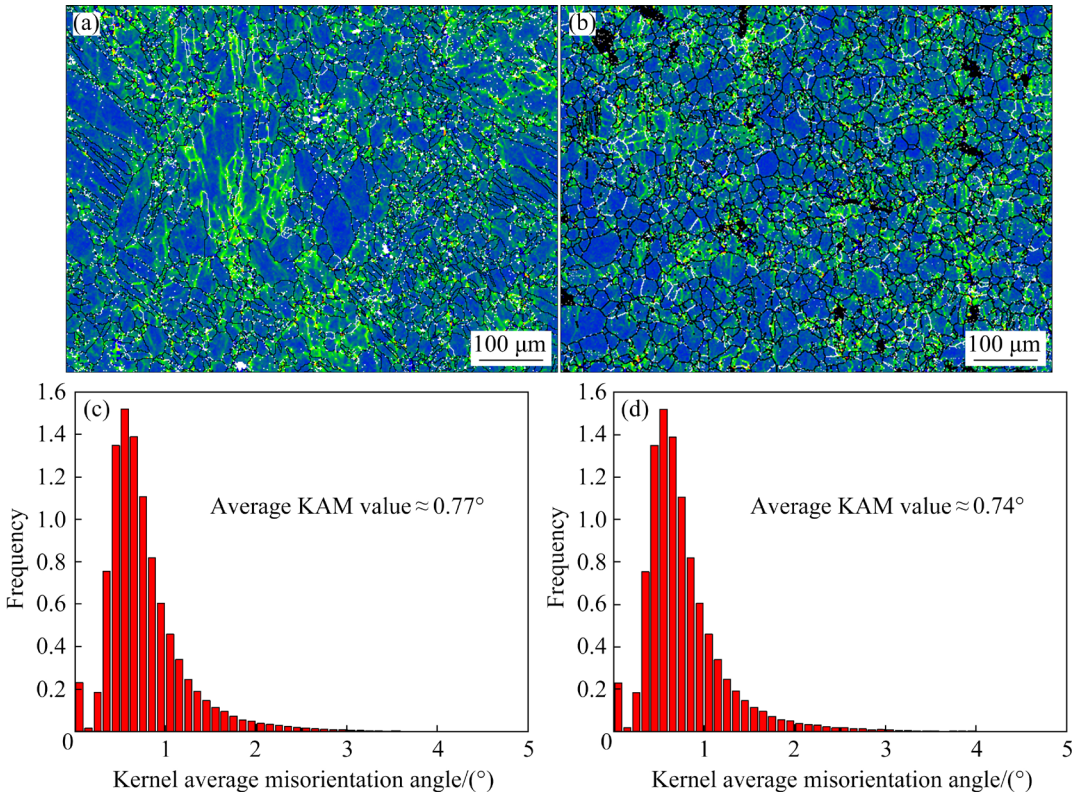

Fig. 6 Morphologies (a, b) and KAM results (c, d) of ECAP-treated ZX11 alloys: (a, c) 1 pass; (b, d) 4 passes

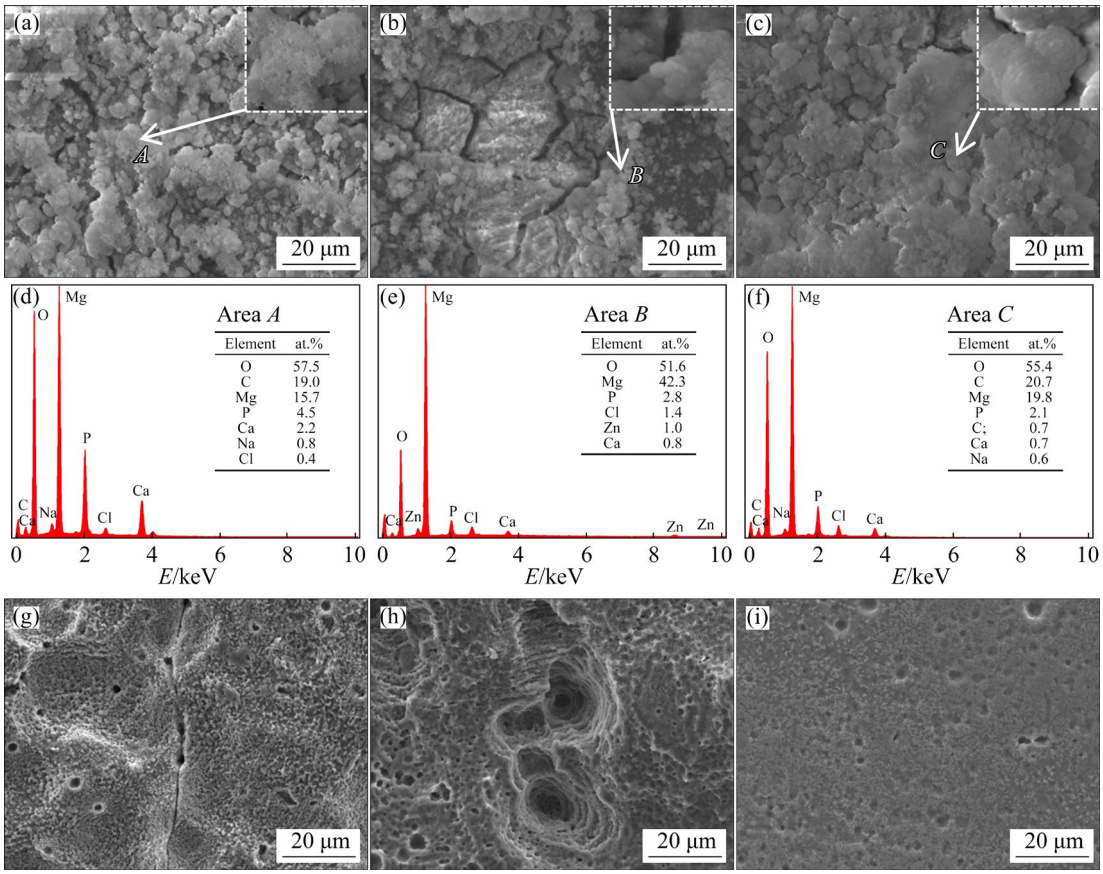

Fig. 7 Corrosion morphologies of ZX11 alloys after immersion in SBF for 3 d (a−c), EDS results (d−f) of Points *A*−*C* in (a, b), respectively, and morphologies after removal of corrosion products (g−i): (a, g) As-cast; (b, h) 1 pass; (c, i) 4 passes

(Fig. 7(a)). For the ECAP-1 pass-treated alloy, corrosion morphology is not uniform and corrosion product film is not dense, the corrosion cracks distributed along grain boundaries are more pronounced (Fig. 7(b)), which make the alloy more susceptible to internal erosion. The surface of the ECAP-4 passes-treated alloy (Fig. 7(c)), displayed thick and dense corrosion product films and no cracks were observed on its surface. The EDS results showed that the corrosion products consisted mainly of O, Mg, C, P and Ca, with small amounts of Na and Cl (Figs. 7(d−f)). The spherical corrosion product (Point *B* in Fig. 7(b)) had an atomic ratio of Mg to O close to 1∶1, which suggested that it was composed of MgO. The blocky corrosion products (Points *A* and *C* in Figs. 7(a) and (c)) had a relatively high O content and contained Mg, P, Ca, and other elements. When the ZX11 alloy was immersed in SBF, corrosion products were generated according to reactions of Eqs. (2)−(8) [22]:

$$\text{Anodic reaction: } Mg \rightarrow Mg^{2+}+2e \quad (2)$$

$$\text{Cathodic reaction: } 2H_2O+2e \rightarrow H_2+2OH^- \quad (3)$$

$$Mg^{2+}+2OH^- \rightarrow Mg(OH)_2 \quad (4)$$

$$HCO_3^-+OH^- \rightarrow CO_3^{2-}+H_2O \quad (5)$$

$$H_2PO_4^-+OH^- \rightarrow HPO_4^{2-} \quad (6)$$

$$Ca^{2+}+HPO_4^{2-} \rightarrow CaHPO_4 \quad (7)$$

$$Mg^{2+}+HPO_4^{2-} \rightarrow MgHPO_4 \quad (8)$$

As the anodic and cathodic reactions occur, Mg matrix dissolves to form Mg^{2+} (Eq. (2)) and hydrogen gas and hydroxide ions (Eq. (3)). The Mg^{2+} combines with OH^- to form $Mg(OH)_2$ (Eq. (4)). $Mg(OH)_2$ is initially deposited on the substrate; however, it can be converted into soluble $MgCl_2$ by the Cl^- in SBF. The $H_2PO_4^-$ and HCO_3^- in SBF react with $H_2PO_4^{2-}$ and CO_3^{2-} in an alkaline environment to form HPO_4^{2-} and HCO_3^- (Eqs. (5) and (6)). Based on Eqs. (7) and (8), the blocky corrosion products include $Mg(OH)_2$, MgO, $CaCO_3$, $CaHPO_4$, and $MgHPO_4$.

The corresponding corrosion morphologies after removing the corrosion products are shown in Figs. 7(g−i). For the as-cast alloy, severe corrosion craters are produced at the grain boundaries as shown in Fig. 7(g). The potential of the Mg_2Ca phase was lower than that of the *α*-Mg matrix phase. Therefore, the Mg_2Ca phases corroded preferentially as the anode [23]. Thus, once the Mg_2Ca phase was corroded, the corrosion craters were left at the grain boundaries. The $Ca_2Mg_6Zn_3$, acting as the cathode, forms the galvanic couple with the *α*-Mg matrix. The secondary phases of both $Ca_2Mg_6Zn_3$ and Mg_2Ca distributed within grain boundaries will accelerate galvanic corrosion. The surface of the ECAP-1 pass-treated alloy suffered from dense pitting, and the large pits on the surface indicated severe localized corrosion (Fig. 7(h)). Mg_2Ca distributed at grain boundary has a negative impact on corrosion resistance [24]. The dispersed Mg_2Ca phase fragmented by ECAP (Fig. 2(e)) acts as the anode to be preferentially corroded, and the corrosion spreads rapidly along the grain boundaries, forming continuous corrosion channels. The *α*-Mg matrix eventually loses support and detaches. The surface of the ECAP-4 passes-treated alloy is relatively uniformly smooth and presents no obvious cracks (Fig. 7(i)). This is due to the protective effect of the corrosion product film (Fig. 7(c)). The ECAP-4 passes-treated alloy exhibited the best corrosion resistance.

Figure 8 shows the cross-sectional morphology of the as-cast and ECAP-treated ZX11 alloys. It can be observed that the average thickness of the corrosion product film in as-cast alloy is 53 μm, revealing a characteristic of thin and uneven thickness. For the ECAP-1 pass-treated alloy, the corrosion product film became sparse, and large pits were clearly seen on the substrate because of the insufficient protection from the corrosion product film. However, for the ECAP-4 passes-treated alloy, the corrosion product film became dense and uniform, with an average thickness of 107 μm, which provided better protection to the substrate.

Figure 9 shows the average corrosion rate of as-cast and ECAP-treated ZX11 alloys after immersion in SBF for 7 d, and the corrosion rate was calculated by mass loss [14]. After ECAP 1 pass, the corrosion rate was the highest, reaching 4.2761 mm/a. The corrosion resistance decreased compared with that of the as-cast alloy. However, after ECAP 4 passes, the corrosion resistance increased, which illustrated that different ECAP passes had different effects on the corrosion resistance of the alloy. The reasons for these effects are further explained later.

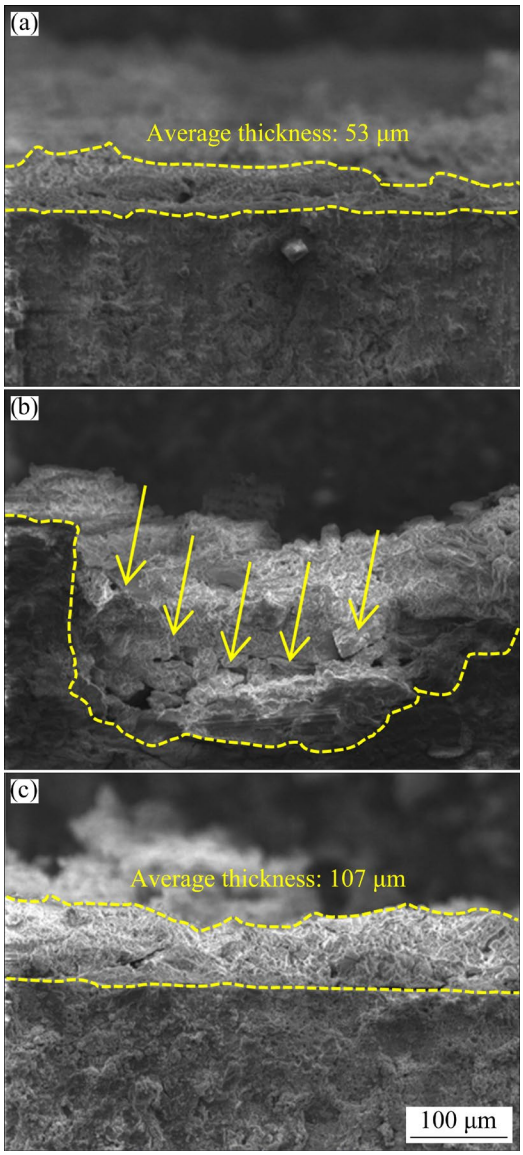

Fig. 8 Cross-sectional morphologies of ZX11 alloys: (a) As-cast; (b) 1 pass; (c) 4 passes

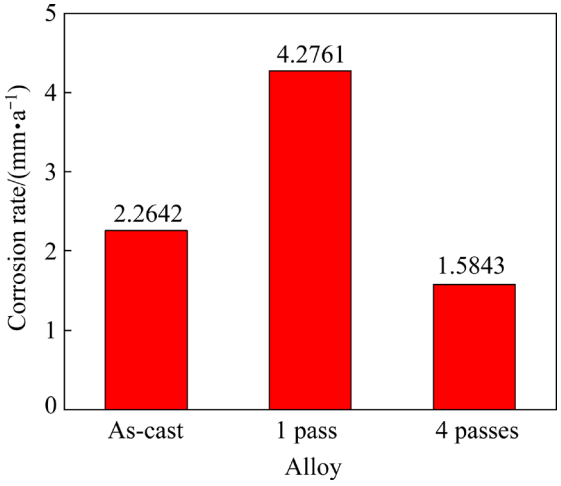

Fig. 9 Average corrosion rates of as-cast and ECAP-treated ZX11 alloys after immersion in SBF for 7 d

3.3 Mechanical properties of ZX11 alloys

Figure 10 shows the tensile curves of the as-cast and ECAP-treated ZX11 alloys. The corresponding yield strength (YS), ultimate tensile strength (UTS), and elongation (EL) values are listed in Table 2. The mechanical properties of the as-cast alloy improved significantly after SPD. After ECAP 1 pass, the YS increased from 50 to 87 MPa, UTS increased from 167 to 202 MPa, and EL increased from 12.5% to 15.0%. The mechanical properties were further optimized after ECAP 4 passes. The YS and UTS increased to 103 and 223 MPa, respectively, and EL increased significantly to 30.5%. According to Fig. 5, the Schmid factor increases after ECAP 4 passes, which should reduce the YS. However, the grains were further refined, and the YS increased to 103 MPa after ECAP 4 passes. According to the Hall−Petch equation [25], decreasing the grain size results in an increase in the YS. This indicates that grain refinement strengthening is the dominant factor in improving the mechanical properties.

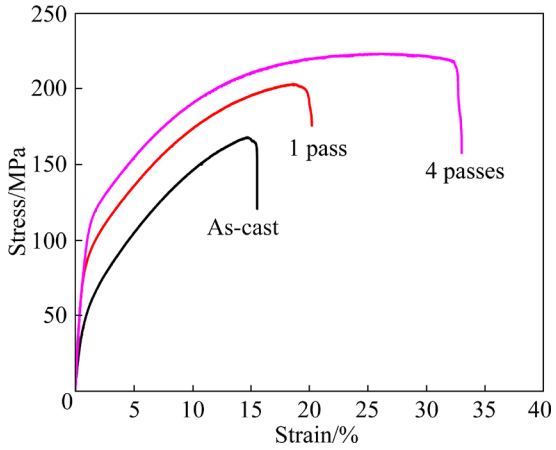

Fig. 10 Tensile curves of as-cast and ECAP-treated ZX11 alloys

Table 2 YS, UTS and EL of alloys

Alloy	YS/MPa	UTS/MPa	EL/%
As-cast	50±1.10	167±1.20	12.5±0.30
1 pass	87±1.40	202±1.30	15.0±0.20
4 passes	103±1.30	223±1.10	30.5±0.30

3.4 Electrochemical properties of ZX11 alloys

Figure 11 illustrates the potentiodynamic polarization (PDP) curves of the as-cast and ECAP-treated ZX11 alloys in SBF. The corrosion current density (J_{corr}), corrosion potential (φ_{corr}), and

polarization resistance (R_p) were obtained from the polarization curves and are listed in Table 3. The corrosion potential ranged from −1.55 to −1.40 V. A higher corrosion potential indicates a lower corrosion tendency [26]. However, the corrosion current density directly determines the corrosion rate and is proportional. In a corrosive system, the anodic current density (J_a) and cathodic current density (J_c) can be expressed by Eqs. (9) and (10):

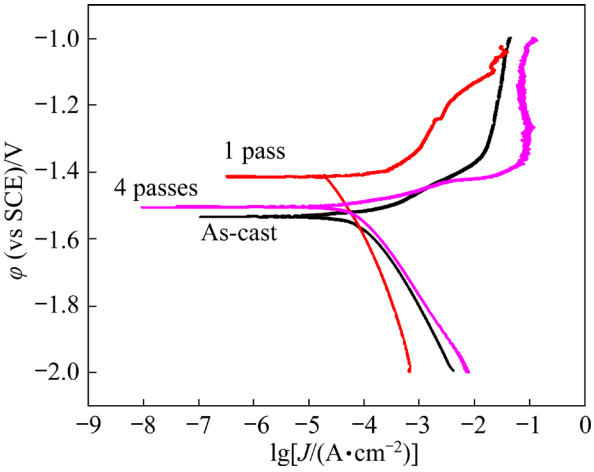

Fig. 11 Potentiodynamic polarization curves of as-cast and ECAP-treated ZX11 alloys in SBF

Table 3 Electrochemical parameters of alloys obtained from polarization curves

Alloy	φ_{corr}(vs SCE)/V	J_{corr}/(μA·cm^{-2})	b_a/(mV·dec^{-1})	b_c/(mV·dec^{-1})	R_p/(Ω·cm^2)
As-cast	−1.5243	103.28	46.31	−272.34	234.88
1 pass	−1.4152	119.43	23.30	−490.17	90.42
4 passes	−1.5063	70.18	44.59	−215.86	348.17

$$J_a = J_a^0 \cdot \exp\left[\frac{2.3(\varphi_{corr} - \varphi_{ae})}{b_a}\right] \quad (9)$$

$$J_c = J_c^0 \cdot \exp\left[\frac{2.3(\varphi_{corr} - \varphi_{ce})}{b_c}\right] \quad (10)$$

where φ_{ae} is the initial anodic potential, φ_{ce} is the initial cathodic potential, b_a is the Tafel anodic slope, and b_c is the Tafel cathodic slope. As corrosion proceeds, the following equation holds when the anode and cathode potentials reach φ_{corr}, as given by

$$J_a = J_c = J_{corr} \quad (11)$$

From Eqs. (9)−(11), we can derive Eq. (12) as

$$J_{corr} = J_a^0 \cdot J_c^0 \frac{b_a b_c}{(b_a + b_c)^2} \times 10^{\frac{\varphi_{ce} - \varphi_{ae}}{b_a + b_c}} \quad (12)$$

Therefore, the corrosion current density is not necessarily related to the corrosion potential but is related to the difference between the initial potentials of the cathode and anode. As such, the corrosion potential is not a reliable indicator of the corrosion rate of the alloy. The corrosion current density of the ECAP-4 passes-treated alloy was the lowest at 70.18 μA/cm^2, and the corrosion current density of the ECAP-1 pass-treated alloy was the highest at 119.43 μA/cm^2. This illustrates that ECAP had a significant effect on the corrosion current density of the alloy. To investigate the corrosion resistance of the ZX11 alloys further, R_p was calculated using Eq. (13) [27]:

$$R_p = \frac{b_a \cdot b_c}{2.3(b_a + b_c) \cdot J_{corr}} \quad (13)$$

Here, b_a and b_c were obtained from the polarization curves. Although the corrosion potential of the ECAP-4 passes-treated alloy was not the highest, it had the highest R_p and the lowest corrosion current density. This implies that the ECAP-4 passes-treated alloy had the lowest corrosion rate. In addition, the alloys showed different anodic polarization behaviors, and the anodic kinetics of the ECAP-4 passes-treated alloy were lower than those of the other two alloys, indicating that the anodic dissolution rate of the alloy decreased after ECAP 4 passes. The cathodic branches of the as-cast alloy and ECAP-4 passes-treated alloy had almost the same slope, but the cathodic curve of ECAP-1 pass-treated alloy was shifted. The behavior of cathodic polarization is linked to the occurrence of the hydrogen evolution reaction [28−30]. In conclusion, according to the fitting results of the polarization curves, the ECAP-4 passes-treated alloy has the greatest corrosion resistance, which is consistent with the immersion test results.

Figure 12 shows the EIS plots of the ZX11 alloys after immersion in SBF. As-cast ZX11 alloy showed a high-frequency capacitive loop, and this high-frequency capacitive loop indicates the charge transfer reaction that occurs at the metal-corrosive medium interface [31]. However, the ECAP-treated alloys showed two capacitive loops, a small loop at

high frequency represents the charge transfer reaction of surface corrosion product/hydroxide film and a large loop at middle frequency charge transfer reaction of electric double layer [32]. R_s is the solution resistance, which should be similar for the same solution (Table 4). R_{ct} is the charge transfer resistance at the interface between the sample and the solution, and R_f is the resistance of the corrosion product film. CPE_{dl} is the charge transfer and double-layer capacitance, and CPE_f is the capacitance of the corrosion product film. A larger capacitive loop in high-frequency and medium-frequency indicates that the charge transfer reaction is more difficult to proceed [33]. As shown in Fig. 12(a), the radii of the ECAP-1 pass-treated alloy capacitive loops at high-frequency and medium-frequency are the smallest, and those of the ECAP-4 passes-treated alloy capacitive loops are the largest. In addition, a higher impedance modulus illustrates a better film stability [34,35]. Figure 12(b) shows that ECAP-4 passes-treated alloy has the largest impedance modulus. The ECAP-4 passes-treated alloy also had the highest R_{ct} and R_f values (Table 4). This indicates that the ECAP-4 passes-treated alloy had better corrosion resistance than the as-cast or ECAP-1 pass-treated alloys, which is consistent with the immersion test results.

3.5 Effect of grain refinement on mechanical properties of ZX11 alloys

The as-cast grains were fractured and twisted by the shear force as the alloy passed through the corner of the die during ECAP. The grain size of ZX11 decreased from 18.46 μm after ECAP 1 pass to 9.24 μm after ECAP 4 passes (Fig. 3). Due to large shear force received by the as-cast grains during ECAP process and dislocation tangle made alloy accumulate a lot of deformation energy; therefore, the refinement effect is significant. DRX occurs easily in Mg alloys because of their low stacking fault energies, which makes it difficult for dislocations to climb [36]. Sub-grains grow into fine DRX grains by sub-grain boundary migration and coalescence. The high dislocation strain energy during shear deformation provides a good driving force and nucleation sites for DRX.

Grain refinement strengthening can improve both the strength and ductility of alloy because grain boundary acts as an obstacle to dislocation motion. The mechanical properties of ZX11 alloys improved with the increasing ECAP passes and reached their optimum values after ECAP 4 passes. However, the Schmid factor also increased from 0.28 to 0.38 with increasing ECAP pass (Fig. 5). This indicates a tendency for the basal slip system to become soft-oriented, which should reduce the

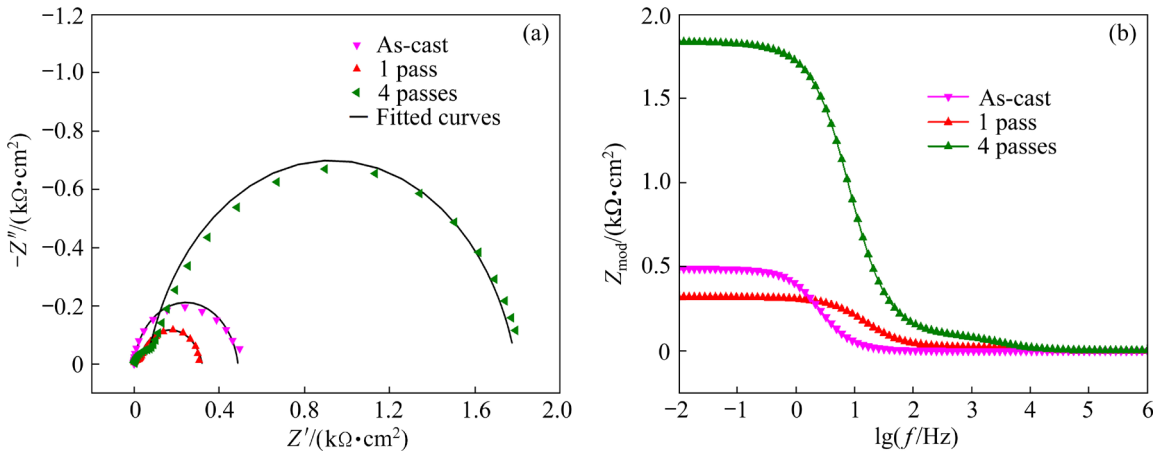

Fig. 12 EIS results of ZX11 alloys after immersion in SBF: (a) Nyquist plot; (b) Bode plot

Table 4 EIS fitting results of alloys

Alloy	R_s/ ($\Omega\cdot cm^2$)	CPE_{dl}		R_{ct}/ ($\Omega\cdot cm^2$)	CPE_f		R_f/ ($\Omega\cdot cm^2$)
		Y/($\mu F\cdot cm^{-2}\cdot s^{n-1}$)	n_{dl}		Y/($\mu F\cdot cm^{-2}\cdot s^{n-1}$)	n_f	
As-cast	12.92	16.72	0.94	489.21			
1 pass	14.66	76.05	0.82	299.41	1.71	0.91	90.03
4 passes	15.15	18.99	0.83	1723.58	2.86	0.82	109.59

YS. In contrast, the YS of ZX11 increased from 87 to 103 MPa after ECAP 4 passes. This can be explained by the Hall−Petch effect, which suggests that a decrease in the grain size leads to an increase in the YS. This confirms that grain refinement strengthening is sufficient to overcome the negative effects of texture softening and is effective in counteracting the soft orientation caused by the texture. With refinement of grains, grain boundaries increased. The number of dislocations accumulating at the boundaries is reduced by the increased pinning points for dislocations at grain boundaries. This will decrease stress concentration and prevent premature crack initiation [37], thereby improving ductility. Moreover, the Schmid factor increased to 0.38, the basal slip can be activated easily, and the alloy will be more prone to coordinated deformation, thus the ductility improved. Its moderate mechanical strength (YS: 103 MPa, UTS: 223 MPa) and higher ductility (EL: 30.5%) are more conducive to the development and practical production of short-term IUDs.

3.6 Effect of grain refinement on corrosion resistance of ZX11 alloys

The corrosion resistance of the as-cast alloy decreased after ECAP 1 pass, as the semi-continuous Mg_2Ca and $Ca_2Mg_6Zn_3$ phases along the grain boundary were fragmented into discrete dots. SONG et al [38] reported that the corrosion rate of the AZ91D Mg alloy increased because of the fragmentation of net-distributed β-phases by plastic deformation. Further, the presence of dispersed galvanic cells formed by discontinuous secondary phases enhanced the galvanic corrosion effect, leading to a decrease in corrosion resistance [39]. After ECAP 1 pass, the alloy underwent significant plastic deformation, resulting in a high dislocation density (Fig. 6(c)). High-density dislocation regions lead to stress concentration, which makes the α-Mg matrix more susceptible to corrosion. All these factors contributed to the decrease in the corrosion resistance of the ECAP-1 pass-treated alloy. The corrosion resistance of the ECAP-4 passes-treated alloy improved significantly compared to that of the as-cast alloy. This can be attributed to the formation of a fine-grain zone, which created a dense corrosion product film on the surface of the alloy. This film acted as a physical barrier, thus improving the corrosion resistance. Schematic diagrams of the corrosion behavior of alloys with different grain sizes are presented in Fig. 13. SPD can increase the number of grain boundaries, which can release the mismatch energy between the substrate and films. This can reduce film cracking by relieving stress and facilitating the formation of denser and more stable corrosion product films on Mg substrates [40]. Consequently, the corrosion resistance can be improved by the physical barrier provided by the corrosion product film. However, a coarse-grained structure can lead to unstable corrosion films that are prone to cracking, allowing the corrosion medium to attack the substrate through cracks in the films (Fig. 13(a)). This explains why the fine-grained structure achieves better corrosion resistance. Corrosion may be suspended until it reaches another grain boundary, where it finds a new preferential direction [41]. The delaying effect of corrosion was more evident when more grain boundaries were present. Thus, the grain boundaries

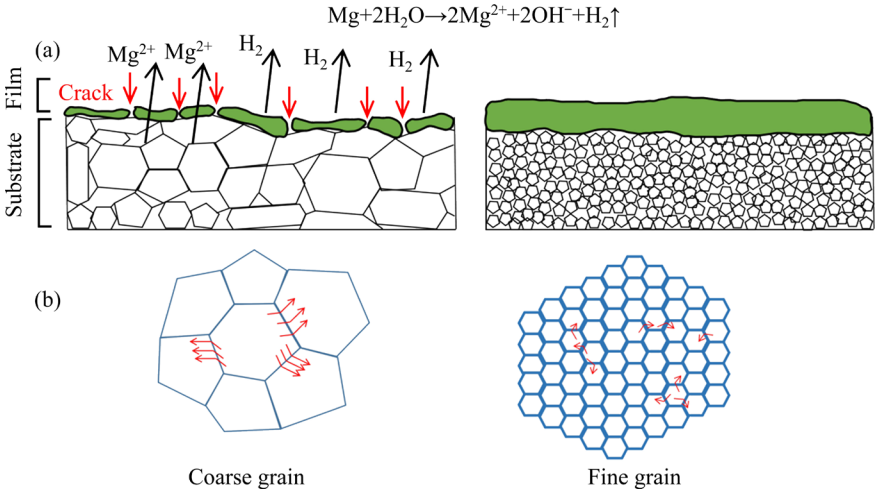

Fig. 13 Schematic diagrams of factors influencing corrosion behavior: (a) Corrosion product films; (b) Grain boundary

acted as barriers to delay corrosion diffusion (Fig. 13(b)). After ECAP 4 passes (Fig. 6(d)), there was a slight decrease in the KAM, but the dislocation density remained high, and the alloy was still sensitive to corrosion. However, the dense corrosion product films and grain boundaries counteracted the negative effect of the dislocations on the corrosion resistance. Therefore, the corrosion resistance of the ECAP-4 passes-treated alloy was improved owing to significant grain refinement, which had a positive impact on the corrosion resistance. In summary, ECAP-4 passes-treating resulted in a simultaneous improvement in the mechanical properties and corrosion resistance of the ZX11 alloy compared to those of the as-cast alloy. The corrosion rate significantly decreased from 4.2761 to 1.5843 mm/a. Due to its lower corrosion rate, this alloy has a tremendous potential as short-term IUDs.

4 Conclusions

(1) The grain size of the ZX11 alloy decreased and the secondary phases at the grain boundary transformed from a semi-continuous network to isolated dots as ECAP pass increased. After ECAP 4 passes, the grain refinement was significant, reaching 9.24 μm.

(2) The ZX11 alloy exhibited remarkable enhancement and optimization of its mechanical properties after ECAP 4 passes. The refined grains resulted in superior strength and ductility, with UTS of 222 MPa, YS of 103 MPa, and EL of 30.5%.

(3) The corrosion resistance of the ZX11 alloy after ECAP 1 pass decreased because of the discontinuous and fragmented Mg_2Ca and $Ca_2Mg_6Zn_3$ phases and the high density of dislocations induced by SPD. However, after ECAP 4 passes, the corrosion resistance increased significantly owing to the formation of dense corrosion product films by the fine-grained zone and the grain boundary acting as a barrier for corrosion.

CRediT authorship contribution statement

Yi-zhuo WANG: Investigation, Formal analysis, Data curation, Writing − Original draft; **Xiao-ping LUO:** Data curation, Methodology, Writing − Review & editing; **Guang-xiao REN:** Software, Visualization; **Hong-xia WANG:** Conceptualization, Validation, Writing − Review & editing, Supervision; **Li-fei WANG:** Software, Visualization; **Wei-li CHENG:** Resources, Visualization; **Hang LI:** Resources, Formal analysis; **Xiao-peng LU** and **Kwang-seon SHIN:** Software, Visualization.

Declaration of competing interest

The authors declare that they have no known competing financial interests or personal relationships that could have appeared to influence the work reported in this paper.

Acknowledgments

The authors acknowledge the assistance of Instrumental Analysis Center of Taiyuan University of Technology. This work was financially supported by the National Natural Science Foundation of China (No. 52374395), the Natural Science Foundation of Shanxi Province, China (Nos. 20210302123135, 202303021221143), the Scientific and Technological Achievements Transformation Guidance Special Project of Shanxi Province, China (Nos. 202104021301022, 202204021301009), the Central Government Guided Local Science and Technology Development Projects, China (No. YDZJSX20231B003), the Ministry of Science and Higher Education of the Russian Federation for financial support under the Megagrant (No. 075-15-2022-1133), the National Research Foundation (NRF) grant funded by the Ministry of Science and ICT of Korea through the Research Institute of Advanced Materials (No. 2015R1A2A1A01006795), the China Postdoctoral Science Foundation (No. 2022M710541), and the Research Project supported by Shanxi Scholarship Council of China (No. 2022-038).

References

[1] WU Jiang, TAN Xiao, AN Xu-guang, ZHANG Jing, GUO Yi, LIU Jia, LUO Yuan-qi, YAO Wei-tang, KONG Qing-quan, WANG Qing-yuan. Development of biomedical Ti−Nb−Zr−Mn alloys with enhanced mechanical properties and corrosion resistance [J]. Materials Today Communications, 2022, 30: 103027.

[2] LI Juan, SUO Jin-ping, HUANG Xu-bin, JIA Lin-tao. Study on a novel copper-containing composite for contraception [J]. Contraception, 2009, 79: 439−444.

[3] WANG Gao-qi, WANG Shou-ren, YANG Xue-feng, WEN Dao-sheng, GUO Yu. Microstructure, mechanical properties and fretting corrosion wear behavior of biomedical ZK60 Mg alloy treated by laser shock peening [J]. Transactions of Nonferrous Metals Society of China, 2023, 33: 1715−1728.

[4] WITTE F. The history of biodegradable magnesium implants: A review [J]. Acta Biomaterialia, 2010, 6: 1680−1692.

[5] ZHOU Hang, LIANG Bing, JIANG Hao-tao, DENG Zhong-liang, YU Ke-xiao. Magnesium-based biomaterials as

emerging agents for bone repair and regeneration: From mechanism to application [J]. Journal of Magnesium and Alloys, 2021, 9: 779−804.

[6] JIA Qing-gong, ZHANG Wen-xin, SUN Yi, XU Chun-xiang, ZHANG Jin-shan, KUAN Jun. Microstructure and mechanical properties of as-cast and extruded biomedical Mg−Zn−Y−Zr−Ca alloy at different temperatures [J]. Transactions of Nonferrous Metals Society of China, 2019, 29: 515−525.

[7] DING De-yu, DU Yu-hang, TANG Mei-fang, SONG Bo, GUO Ning, ZHANG Hong-ju, GUO Sheng-feng. Corrosion and discharge behavior of Mg−Zn−Mn−Nd alloys as primary Mg−air batteries anode [J]. Transactions of Nonferrous Metals Society of China, 2023, 33: 2014−2029.

[8] GUAN Kai, ZHANG Jing-huai, YANG Qiang, LI Bai-shun, WU Rui-zhi, MENG Jian. Effects of trace Ca addition on microstructure and mechanical properties of as-cast Mg−Sm−Gd-based alloy [J]. Transactions of Nonferrous Metals Society of China, 2023, 33: 46−58.

[9] SINGH C, PANDA S S, SINGH S S, JAIN J. Development of sustainable novel Mg−Ca−Sc alloys with exceptional corrosion resistance [J]. Journal of Alloys and Compounds, 2023, 955: 170251.

[10] GU Xue-nan, ZHENG Yu-feng, CHENG Yan, ZHONG Shen-ping, XI Ting-fei. In vitro corrosion and biocompatibility of binary magnesium alloys [J]. Biomaterials, 2009, 30: 484−498.

[11] PALSTON K D, BIRBILIS N, DAVIES C H J. Revealing the relationship between grain size and corrosion rate of metals [J]. Scripta Materialia, 2010, 63: 1201−1204.

[12] TORKIAN A, FARAJI G, PEDRAM M S. Mechanical properties and in vivo biodegradability of Mg−Zr−Y−Nd−La magnesium alloy produced by a combined severe plastic deformation [J]. Rare Metals, 2021, 40: 651−662.

[13] GUI Zhen-zhen, KANG Zhi-xi, LI Yuan-yuan. Mechanical and corrosion properties of Mg−Gd−Zn−Zr−Mn biodegradable alloy by hot extrusion [J]. Journal of Alloys and Compounds, 2016, 685: 222−230.

[14] LIU Ke, LOU Feng, FU Jun-jian, YU Zi-jian, LI Shu-bo, WANG Zhao-hui, DU Xian, DU Wen-bo. Microstructure and corrosion behaviors of as-rolled Mg−Zn−Er alloy sheets [J]. Transactions of Nonferrous Metals Society of China, 2022, 32: 1881−1895.

[15] MINETA T, SUZUMURA R, KONYA A, SATO H. Effect of strain-induced grain boundary migration on microstructure and creep behavior of extruded AZ31 magnesium alloy prepared by pre-compression and annealing treatment [J]. Materials Today Communications, 2023, 34: 105502.

[16] JIN Wei-hang, WU Bao-lin, ZHANG Li, WAN Gang, ZHANG Lu, TANG Yan, DUAN Guo-sheng. Twinning character and texture origination in the randomly-oriented AZ31B magnesium alloy during cold-rolling [J]. Journal of Materials Research and Technology, 2022, 19: 151−166.

[17] ZHENG Liu-wei, ZHANG Xiang-peng, WANG Hong-xia, WANG Li-fei, HOU Hua, LI Hang, SHIN Kwang-seon. Synergistic effect of LPSO and eutectic phase on mechanical properties of Mg−Gd−Nd−Zn−Zr alloy during equal channel angular pressing [J]. Journal of Materials Research and Technology, 2021, 15: 2459−2470.

[18] SÁNCHEZ-MARTÍN R, PÉREZ-PRADO M T, SEGURADO J, BOHLEN J, GUTIÉRREZ-URRUTIA I, LLORCA J, MDLINA-ALDAREGUIA J M. Measuring the critical resolved shear stresses in Mg alloys by instrumented nanoindentation [J]. Acta Materialia, 2014, 71: 283−292.

[19] KASAEIAN-NAEINI M, SEDIGHI M, HASHEMI R. Severe plastic deformation (SPD) of biodegradable magnesium alloys and composites: A review of developments and prospects [J]. Journal of Magnesium and Alloys, 2022, 10: 938−955.

[20] XU Shi-wei, ZHU Cong-cong, KAMADO S, OH-ISHI K, QIN Yun. Dynamic recrystallization behavior of as-cast AZ91 magnesium alloy during hot compressive [J]. Journal of Materials Research and Technology, 2022, 18: 5116−5125.

[21] GUO Ming, ETIM P, YANG Ke, TAN LI-li, MA Zheng. Enhancing mechanical property and corrosion resistance of Mg−Zn−Nd alloy wire by a combination of SPD techniques, extrusion and hot drawing [J]. Materials Science and Engineering: A, 2022, 829: 142058.

[22] RAD H R B, IDRIS M H, KADIR M R A, FARAHANY S. Microstructure analysis and corrosion behavior of biodegradable Mg−Ca implant alloys [J]. Materials & Design, 2012, 33: 88−97.

[23] LIU Yi-chi, LIU De-bao, ZHAO Yue, CHEN Min-fang. Corrosion degradation behavior of Mg−Ca alloy with high Ca content in SBF [J]. Transactions of Nonferrous Metals Society of China, 2015, 25: 3339−3347.

[24] HE Shu-heng, WANG Ce, SUN Chao, ZHANG Yue, YAN Kai, JIANG Jing-hua, BAI Jing, XUE Feng, LIU Huan. Corrosion properties of ECAP-processed Mg−Al−Ca−Mn alloys with separate Al_2Ca and Mg_2Ca phases [J]. Transactions of Nonferrous Metals Society of China, 2022, 32: 2527−2540.

[25] SOMEKAWA H, MUKAI T. Hall−Petch relation for deformation twinning in solid solution magnesium alloys [J]. Materials Science and Engineering: A, 2013, 561: 378−385.

[26] YANG Zhen-quan, MA Ai-bin, XU Bing-qian, JIANG Jing-hua, SUN Jia-peng. Corrosion behavior of AZ91 Mg alloy with a heterogeneous structure produced by ECAP [J]. Corrosion Science, 2021, 187: 109517.

[27] ARGADE G R, KANDASAMY K, PANIGRAHI S K, MISHRA R S. Corrosion behavior of a friction stir processed rare-earth added magnesium alloy [J]. Corrosion Science, 2012, 58: 321−326.

[28] LIU Qu, MA Qing-xian, CHEN Gao-qiang, CAO Xiong, ZHANG Shuai, PAN Ji-luan, ZHANG Gong, SHI Qing-yu. Enhanced corrosion resistance of AZ91 magnesium alloy through refinement and homogenization of surface microstructure by friction stir processing [J]. Corrosion Science, 2018, 138: 284−296.

[29] LI Feng, CHENG Wei-li, YU Hui, WANG Hong-xia, NIU Xiao-feng, Li-fei WANG, LI Hang, HOU hua. Corrosion behavior and mechanical properties of extruded low-alloyed Mg−0.5Bi−0.5Y−0.2Zn alloy [J]. Transactions of Nonferrous Metals Society of China, 2023, 33: 743−754.

[30] CUBIDES Y, ZHAO De-xin, NASH L, YADAV D, XIE K, KARAMAN I, CASTANEDA H. Effects of dynamic

recrystallization and strain-induced dynamic precipitation on the corrosion behavior of partially recrystallized Mg−9Al−1Zn alloys [J]. Journal of Magnesium and Alloys, 2020, 8: 1016−1037.

[31] LI Mei-xuan, WANG Cheng, LI Yi-jia, WANG De-wei, ZHA Min, GAO Yi-peng, WANG Hui-yuan. Tailoring the microstructure and enhancing the corrosion resistance of extruded dilute Mg−0.6Al−0.5Mn−0.25Ca alloy by adding trace Ce [J]. Corrosion Science, 2022, 207: 110605.

[32] ZHANG Kai, WANG Cheng, LIU Shi, GUAN Kai, LI Mei-xuan, ZHANG Lin-yang, WANG Hui-yuan. New insights on corrosion behavior of aging precipitates in dilute Mg−Al−Ca alloy by experiments and first-principles calculations [J]. Corrosion Science, 2023, 220: 111254.

[33] ZHANG C Z, ZHU S J, WANG L G, GUO R M, YUE G C, GUAN S K. Microstructures and degradation mechanism in simulated body fluid of biomedical Mg−Zn−Ca alloy processed by high pressure torsion [J]. Materials & Design, 2016, 96: 54−62.

[34] XI Guo-qiang, MOU Yu, MA Yan-long, ZHAO Xu-hang, XIONG Ju, MA Kai, WANG Jing-feng. Effect of volume fraction of 18R-LPSO phase on corrosion resistance of Mg−Zn−Y alloys [J]. Transactions of Nonferrous Metals Society of China, 2023, 33: 454−466.

[35] LIU Xu-xiang, CURIONI M, LIU Zhu. Correlation between electrochemical impedance measurements and corrosion rates of Mg−1Ca alloy in simulated body fluid [J]. Electrochimica Acta, 2018, 264: 101−108.

[36] GUAN Di-kai, RAINFORTH W, GAO Jun-heng, SHARP J, WYNNE B, MA Le. Individual effect of recrystallisation nucleation sites on texture weakening in a magnesium alloy: Part 1. Double twins [J]. Acta Materialia, 2017, 135: 14−24.

[37] SUN Chao, LIU Huan, XU Zi-yue, WU Yu-na, YAN Kai, JU Jia, JIANG Jing-hua, XUE Feng, BAI Jing, XIN Yun-chang. Refining 18R-LPSO phase into sub-micron range by pre-kinking design and its prominent strengthening effect on $Mg_{97}Y_2Zn_1$ alloy [J]. Journal of Materials Science & Technology, 2024, 176: 13−24.

[38] SONG D, MA A B, JIANG J H, LIN P H, YANG D H, FAN J F. Corrosion behaviour of bulk ultra-fine grained AZ91D magnesium alloy fabricated by equal-channel angular pressing [J]. Corrosion Science, 2011, 53: 362−373.

[39] BAHMANI A, LOTFPOUR M, TAGHIZADEH M, KIM Woo-jin. Corrosion behavior of severely plastically deformed Mg and Mg alloys [J]. Journal of Magnesium and Alloys, 2022, 10: 2607−2648.

[40] SIAHSARANI A, FARAJI G. Processing and characterization of AZ91 magnesium alloys via a novel severe plastic deformation method: Hydrostatic cyclic extrusion compression (HCEC) [J]. Transactions of Nonferrous Metals Society of China, 2021, 31: 1303−1321.

[41] HAN Gilsoo, LEE Ji-young, KIM Yu-chan, PARK Ji-hee, KIM Dong-ik, Han Hyung-seop, YANG Seok-jo, SEOK Hyun-kwang. Preferred crystallographic pitting corrosion of pure magnesium in Hanks' solution [J]. Corrosion Science, 2012, 63: 316−322.

采用等通道转角挤压通过晶粒细化同步提高 Mg−Zn−Ca 合金的耐腐蚀性能和力学性能

王艺卓[1]，罗小萍[2]，任广笑[3]，王红霞[1]，王利飞[1]，程伟丽[1]，李 航[1]，鲁小鹏[4]，Kwang-seon SHIN[5]

1. 太原理工大学 山西省镁基材料重点实验室 材料科学与工程学院，太原 030024；
2. 太原科技大学 材料科学与工程学院，太原 030024；
3. 山西江淮重工有限责任公司，晋城 048000；
4. 东北大学 材料科学与工程学院，沈阳 110819；
5. Magnesium Technology Innovation Center, School of Materials Science and Engineering, Seoul National University, Gwanak-ro, Gwanak-gu, Seoul 08826, South Korea

摘 要：为了研究显微组织演变对 Mg−1Zn−1Ca (质量分数，%)合金腐蚀行为和强化机制的影响，对铸态 Mg−1Zn−1Ca 合金分别进行 1 道次和 4 道次等通道转角挤压(ECAP)。通过光学显微镜(OM)、扫描电子显微镜(SEM)、电子背散射衍射(EBSD)、电化学试验、浸泡试验和拉伸试验研究合金的腐蚀行为和力学性能。结果表明，ECAP 1 道次挤压后，力学性能得到改善，但耐腐蚀性能下降，这是由于 ECAP 挤压产生了高密度位错和破碎的第二相。合金经过 ECAP 4 道次挤压后通过细化晶粒实现了力学性能和耐腐蚀性的同步提升，细晶粒使屈服强度、极限抗拉强度、伸长率和腐蚀速率显著提高，分别达到 103 MPa、223 MPa、30.5%和 1.5843 mm/a，耐腐蚀性能的增强归因于细晶粒形成致密的腐蚀产物膜以及高密度晶界对腐蚀的阻挡效应。这表明 Mg−1Zn−1Ca 合金在生物医学材料中具有广阔的应用前景。

关键词：Mg−1Zn−1Ca 合金；等通道转角挤压；晶粒细化；腐蚀行为；力学性能

(Edited by Xiang-qun LI)